Prediction of the reaction yield in a X-micromixer given the mixing degree and the kinetic constant

S. Tomasi Masoni ®, A. Mariotti ®,* M. Antognoli ®, C. Galletti ®, R. Mauri ®,
M. V. Salvetti ®, and E. Brunazzi ®
Dipartimento di Ingegneria Civile e Industriale, University of Pisa, 56122 Pisa, Italy

An adequate comprehension of the flow regimes and mixing process inside microreactors is a crucial factor to obtain high reaction yields. In the present paper, we carry out jointly simulations and experiments to characterize the flow regimes and reaction occurring in a X-microreactor up to Reynolds number, Re, based on the inlet bulk velocity and mixing channel hydraulic diameter, equal to 600. For Re > 375, an unsteady periodic regime is found, characterized by the presence of a central vortical flow structure that periodically collapses leading to symmetric vorticity shedding in both outlet channels. In the meanwhile, two counterrotating vortices form in the confluence region of the inlet streams, come closer, and merge creating again the central vortex. Compared to the steady engulfment regime, previously described in the literature and characterized by a single steady central vortex, a higher mixing degree is found in the unsteady regime. However, despite the increased mixing, the reaction yield remains similar, as the enhanced mixing is counterbalanced by the reduced residence time of the reactants. Based on the obtained results we developed a model to predict the reaction yield, given the mixing degree and the nominal kinetic constant as input data. The proposed law successfully predicts the reaction yield in all the flow regimes, including the unsteady engulfment one regime, and for the Damköhler numbers in the range $10^{-1} <$ Da $< 10^3$ (chemistry slower and faster than flow convection).

I. INTRODUCTION

The miniaturization of the chemical and biochemical processes has gained increasing interest in the pharmaceutical industry and fine chemistry, for the intensification of reaction selectivity and product quality. Microreactor technology enhances heat and mass transfer, leading to a better control of the operating conditions compared to the traditional batch-stirred reactors [1,2]. Indeed, the fluid flow in milli and microreactors can be manipulated more accurately than in conventional batch reactors [3–6], and it is possible to use less diluted or even solvent-free solutions, thus promoting more sustainable and affordable approaches [7]. In this framework, microfluidics can be successfully applied to improve diagnostics and biology research [8], to enhance mixing and yield of chemical reactions [9,10], to properly control droplet generation and particle size distribution in pharmaceutics and cellular analysis [11–14], and to enhance seeding and growth control in continuous cristallization [15].

Among the simplest devices, T-, arrow-, and X-micromixers are suggested [16–19]. Flow regimes in these microreactors have been extensively studied by considering different fluid properties [20–22], cross-sectional geometries [23–25], channel aspect ratios [26,27]. Design changes in the mixing channel have been proposed, such as a serpentine microchannel [28], a split-and-recombine
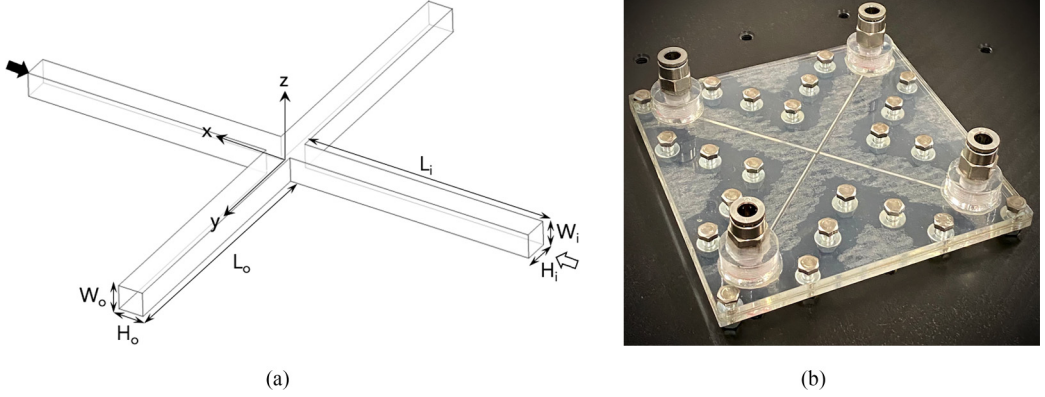
---

*alessandro.mariotti@unipi.it

FIG. 1. (a) Geometry of the X-microreactor and (b) experimental device.

mixer [29], or a sequence of obstacles or cavities inserted inside the devices to promote mixing [30–33].

We focus herein on the reaction performance in a X-shaped microdevice in the configuration 2-inlets and 2-outlets. Several studies have been devoted to characterize the flow regimes occurring in a X-micromixer using water as a working fluid [34–37], as it is retained to be more efficient than the T-shaped one [16]. At low Reynolds numbers, Re, Zhang *et al.* [36] observed the two streams coflowing in both the outlet channels. By increasing Re, steady engulfment regime occurs, characterized by the formation of a central vortex that breaks the symmetric pattern and significantly enhances the mixing efficiency [20,38]. Keeping increasing the Reynolds number, the flow becomes unsteady and time-periodic [36]. The central vortex, typical of the steady engulfment regime, breaks and symmetrically splits in two parts into the outlet channels. At the same time, from the impinging flow, two corotating vortices form again and during the cycle, they merge in the confluence region, leading to the reformation of a single central vortex.

Recently, we started to investigate the performance of a X-microreactor through simulations and experiments in steady flow regimes. The selected test reaction consists of the reduction of the methylene blue (MB^+) by ascorbic acid (AsA) and catalyzed by hydrogen chloride (HCl). This reaction was selected because the progress can be associated with the decolorization of the limiting reagent MB^+, which can be measured through experimental flow visualizations [39–41]. In addition, the reaction kinetics can be modulated by varying the concentration of HCl. Steady flow regimes occurring for reactive streams are similar to those found for water even if the stratification effect is present because of the different density of the two streams [41]. Moreover, the performance of the X-microreactor for different kinetic constants was analyzed in Ref. [41], showing that the reaction yield is very high even if the kinetic constant is low. The high reaction yields achieved in the steady regimes motivate a further analysis at higher Reynolds numbers, which, to the best of our knowledge, is not available in the open literature.

The aim of the paper is twofold. First, we want to extend the results of [41] up to Re = 600 for the same reaction rates through simulations and experiments. Then, for all the flow regimes we intend to analyze the relationship between the flow features, the kinetics, and the reaction yields and develop an analytic model to predict the reaction yield given the mixing degree and the kinetic constant.

II. EXPERIMENTAL SETUP AND TEST REACTION

The X-microreactor is sketched in Fig. 1. It presents four identical channels in impinging jet configuration [20,41]. Each channel has a square cross-section with dimensions $W_i = W_0 = H_i = H_0 = 1$ mm. Thus, the hydraulic diameter is $d = 1$ mm. Fully developed flow in the confluence

TABLE I. Kinetic constant $k_{r,0}$ evaluated for the nominal HCl concentrations.

HCl [mol/l]	$k_{r,0}$ [1/s]
0.1	2.60
1.00	10.71
2.19	21.43
5.36	50.00

region is guaranteed with a length of $L_i = L_0 = 60\,d$ [42]. The microreactor is constructed with three sealed layers of polymethylmethacrylate (PMMA), with the central layer (1 mm thick) having an X-shape cut.

The chosen test reaction is the reduction of methylene blue (MB^+) to the colorless leucomethylene blue (LMB^+) using ascorbic acid (AsA). Hydrogen chloride (HCl) is the catalyst of the reaction:

$$MB^+ + AsA \xrightarrow{HCl} LMB^+ + DA, \tag{1}$$
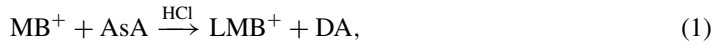
where DA is the dehydroascorbic acid.

The kinetic of this reaction, studied by Mowry and Ogren [43], follows a pseudo-first-order law in excess of ascorbic acid (see Refs. [40,44] for more details):

$$\frac{d[MB^+]}{dt} = \frac{d[AsA]}{dt} = -\frac{d[DA]}{dt} = -\frac{d[LMB^+]}{dt} = -k_r[MB^+]; \quad \frac{d[HCl]}{dt} = 0, \tag{2}$$

The kinetic constant k_r may be written as

$$k_r = (k_0 + k_1[HCl])[AsA], \tag{3}$$

with $k_0 = 1\,\mathrm{l\,mol^{-1}\,s^{-1}}$ and $k_1 = 5.3\,\mathrm{l^2\,mol^{-2}\,s^{-1}}$.

The two inlet channels are supplied with an aqueous solution of MB^+ and HCl and an aqueous solution of AsA, respectively. To obtain the former solution, we dissolve $[MB^+] = 5.33 \times 10^{-5}$ mol/l powder (by Sigma Aldrich) in hydrochloric acid. The physical properties of these solutions may be assumed to be analogous to those of pure water. The other solution is made by dissolving L-ascorbic acid (Ultrafine vitamin C powder by Cutatonic), with a concentration of $[AsA] = 1.7$ mol/l, in deionized water. This solution has $\rho = 1.117\,\mathrm{g/cm^3}$, $\mu = 1.7\,\mathrm{mPa \times s}$ and $\nu = 1.52\,\mathrm{mm^2 s}$. In our analysis, we consider four different concentrations of HCl, while only one concentration of ascorbic acid is considered; thus, $k_r = k_{r,0}$ for $[AsA] = 1.7$ mol/l. Table I shows the kinetic constant $k_{r,0}$ evaluated from Eq. (3) for the four nominal HCl concentrations.

A syringe pump (model Gemini 88 by KD Scientific) injects the inlet streams into the microreactor using two plastic syringes of 60 ml (Becton Dickson). Both solutions are fed at the same bulk velocity, U.

The flow in the microdevice is seen though an upright microscope (Eclipse 80 by Nikon). The microscope has a $4\times$ magnifying lens with N.A. $= 0.13$. Images are obtained using an high-speed camera (Velociraptor HS by Optomotive). The monochrome sensor of the camera is square with 2048×2048 pixels. Its maximum frame rate for full sensor is equal to 174 frames/s. For the present experiment, a rectangular subpart of the sensor is chosen (550×2048 pixels), allowing us to reach a frame rate of 1300 frames/s. A $0.5\times$ lens is placed in front of the sensor to obtain a field view region of $1.6d \times 6d$ in a single image. In each image, a pixel corresponds to 2.93 μm.

The sensor of the camera captures an intensity of the light, which depends solely on the methylene blue concentration, the only light-absorbing component of the solution. The Lambert-Beer law is applied to each (i, j)th pixel to transform the light intensity images into normalized

distributions of MB$^+$ concentration.

$$\frac{\ln(L_{\text{blank},ij}) - \ln(L_{ij})}{\ln(L_{\text{blank},ij}) - \ln(L_{\text{max},ij})} = \frac{C_{ij}}{C_0} \quad (4)$$

where, L_{ij} is the light intensity with MB$^+$ concentration equal to C_{ij}, $L_{\text{blank},ij}$ the light intensity for the blank solution only, and $L_{\text{max},ij}$ is the maximum light intensity of the solution with MB$^+$ concentration equal to $C_0 = 5.33 \times 10^{-5}$ mol/l. Additional details on the calibration and post-processing of the acquired images are provided in Refs. [40,45].

The refractive index of the two streams differs slightly; it is approximately 1.33 for the MB$^+$ solution and 1.36–1.37 for the ascorbic acid solution [46]. Consequently, optical rays experience deviation in their path through the specimen due to the refractive index disparity between the two solutions. This deviation results in the observation of darker or brighter streaks at the contact fronts of the two fluids, compared to the rest of the image. Following the procedure outlined in Ref. [40], precise adjustment of the condenser's height in relation to the objective, as well as aperture adjustments for both the condenser and field diaphragms, enabled us to either minimize streak presence in the collected images (which could otherwise affect concentration measurements during reaction yield visualizations) or intentionally emphasize the streaks. This deliberate highlighting of streaks allows for the visualization of flow topology and vortical structures.

III. NUMERICAL METHODOLOGY

Navier-Stokes equations are solved together with the transport/reaction equations for all the chemical species involved in Eq. (1). For the considered reaction, thermal effects are negligible and, accordingly, the energy equation is not involved. Thus, the equations defining the problem are

$$\frac{\partial \hat{\rho}}{\partial \theta} + \boldsymbol{\nabla} \cdot (\hat{\rho} \mathbf{v}) = 0, \quad (5)$$

$$\hat{\rho} \left(\frac{\partial \mathbf{v}}{\partial \theta} + \mathbf{v} \cdot \boldsymbol{\nabla} \mathbf{v} \right) = -\boldsymbol{\nabla} p + \frac{1}{\text{Re}} \boldsymbol{\nabla} \cdot [\hat{\mu}(\boldsymbol{\nabla} \mathbf{v} + \boldsymbol{\nabla} \mathbf{v}^T)] + Ri(\hat{\rho} - 1)\hat{\mathbf{g}}, \quad (6)$$

$$\hat{\rho} \left(\frac{\partial \phi_k}{\partial \theta} + \mathbf{v} \cdot \boldsymbol{\nabla} \phi_k \right) = \frac{1}{Pe} \boldsymbol{\nabla} \cdot (\hat{\rho} \hat{\mathcal{D}}_k \boldsymbol{\nabla} \phi_k) + \frac{d\dot{\omega}_k}{\rho_0 U}, \quad (7)$$

where we use the hydraulic diameter of the channels d and inlet bulk velocity U as reference quantities in making the equations nondimensional. Consequently, the time in its nondimensional form is $\theta = \frac{tU}{d}$. The dimensionless velocity vector is $\mathbf{v}$, the modified dimensionless pressure is $p = (P - \rho_0 gz)/\rho_0 U^2$, where P is the dimensional pressure, and the dimensionless gravity acceleration is $\hat{\mathbf{g}} = \frac{\mathbf{g}}{g}$. Dimensionless density and viscosity are $\hat{\rho} = \rho/\rho_0$ and $\hat{\mu} = \mu/\mu_0$, referred to the values for pure water at $20°$C (ρ_0 and μ_0). The mass fraction of the kth chemical species is indicated with ϕ_k and its rate consumption/production in chemical reactions is $\dot{\omega}_k$ (e.g., for the methylene blue $\dot{\omega}_{\text{MB}^+} = -k_r \rho \phi_{\text{MB}^+}$). Finally, the nondimensional diffusivity is $\hat{\mathcal{D}}_k = \mathcal{D}_k/\mathcal{D}_0$, again referred to pure water ($\mathcal{D}_0$). The following dimensionless numbers define the problem: the Reynolds $\text{Re} = \frac{\rho_0 U d}{\mu_0}$, the Richardson $\text{Ri} = \frac{gd\,\Delta\rho}{\rho_0 U^2}$, and the Peclet $\text{Pe} = \frac{Ud}{\mathcal{D}_0}$ numbers, where $\Delta\rho$ is the difference between the densities of the two feeding solutions.

The Damköhler number, Da$_k$, indicates the ratio between the characteristic time of the convection and that of the chemical reaction for the kth species:

$$\text{Da}_k = \frac{d\dot{\omega}_k}{U\rho\phi_k}. \quad (8)$$

If we considered, for instance, the methylene blue reduction, i.e., $k = \text{MB}^+$ and $\text{Da}_{\text{MB}^+} = d\dot{\omega}_{\text{MB}^+}/U\rho\phi_{\text{MB}^+} = dk_r/U$. We can also define a nominal Damköhler number for each of the

considered HCl concentrations as follows:

$$\mathrm{Da} = dk_{r,0}/U, \tag{9}$$

where $k_{r,0}$ is the kinetic constant in nominal conditions (see Table I).

Consequently, Eq. (7) for MB$^+$ can be written as

$$\mathbf{v} \cdot \nabla \phi_{\mathrm{MB}^+} = \frac{1}{\mathrm{Pe}} \frac{1}{\hat{\rho}} \nabla \cdot (\hat{\rho} \nabla \phi_{\mathrm{MB}^+}) - \hat{k}_r \mathrm{Da} \phi_{\mathrm{MB}^+}, \tag{10}$$

where $\hat{k}_r = k_r/k_{r,0}$.

Uniform velocity and concentration of the reactants are set as boundary conditions for the two inlet channels, channel walls have no-slip condition, and a reference ambient pressure is set at the two outlets.

Density and viscosity of the the AsA solution are expressed as a function of ϕ_{AsA}, following the correlations described in Ref. [46]:

$$\rho = \rho_0 \big(1 + 0.3970 \, \phi_{\mathrm{AsA}} + 0.1617 \, \phi_{\mathrm{AsA}}^2\big), \tag{11}$$

$$\mu = \mu_0 \big(1 + 1.0605 \, \phi_{\mathrm{AsA}} + 5.7219 \, \phi_{\mathrm{AsA}}^2\big). \tag{12}$$

A second-order upwind interpolation was chosen for spatial discretization, and time advancement was handled with a second-order implicit method with variable time steps corresponding to CFL $\simeq 10$. The segregated SIMPLE algorithm was used for pressure-velocity coupling. The computational domain is discretized with a structured grid having 1.62 M cells; cubical cells are used at the confluence of the channels, while rectangular cells, elongated in the streamwise direction, are placed along the channels. 30×30 square cells are present in the cross-sections of the channels. The independence of the solution from the computational grid has been evaluated in Antognoli *et al.* [20].

IV. MAIN FLOW FEATURES IN THE UNSTEADY ENGULFMENT REGIME

Flow-regime analysis spans Reynolds numbers between Re $= 200$ and Re $= 600$. Since flow-regime features are not affected by the catalyst concentration (the considered range of [HCl] has a negligible influence on the aqueous-solution properties), we show in this Section the results obtained for [HCl] $= 2.19$ mol/l. The steady engulfment regime, also found in Ref. [41] for Re $= 50$–200, occurs until Re $= 375$. Flow features of this regime closely resemble those described for lower Reynolds in Ref. [41], where a central vortex is present at the confluence region, and its strength increases with Reynolds. For Re $= 150$–375, two secondary vortices appear between the central vortex and the channel walls in diametrically opposed position and both counterrotating with respect to the central vortex.

Above Re $= 375$ the flow becomes unsteady and time-periodic with the periodic collapse and formation of the central vortex. Here, to describe the dynamic behavior of the flow in this regime, we consider Re $= 450$ (Figs. 2 and 3) and Re $= 600$ (Figs. 4 and 5).

The flow's temporal evolution can be described as follows by observing the simulation results in Fig. 2. The left panel shows the isosurfaces of the vortex indicator λ_2 [47], while the right panel presents the contours of the nondimensional concentration of MB$^+$ at four cross-sections of the outlet channel at $Y > 0$. Moreover, the vortex cores are highlighted by a dashed line at the $Y = 0.5$ cross-section. The solution containing ascorbic acid enters from the bottom with reference to the left panel, instead the solution of MB$^+$ enters from the top. Eight instants equally spaced in time within a cycle are reported. The cycle time duration is denoted with τ, while the corresponding Strouhal number is defined as St $= \frac{d}{U\tau}$ (St $= 0.06$ for the simulation at Re $= 450$).

As the regime is time-periodic, the initial instant $t/\tau = 0$ is chosen arbitrarily when the central vortex is present in the confluence region together with two corotating lateral vortices, and the flow pattern resemble the one of the steady engulfment regime. Between $t/\tau = 0.25$ and $t/\tau = 0.375$ the
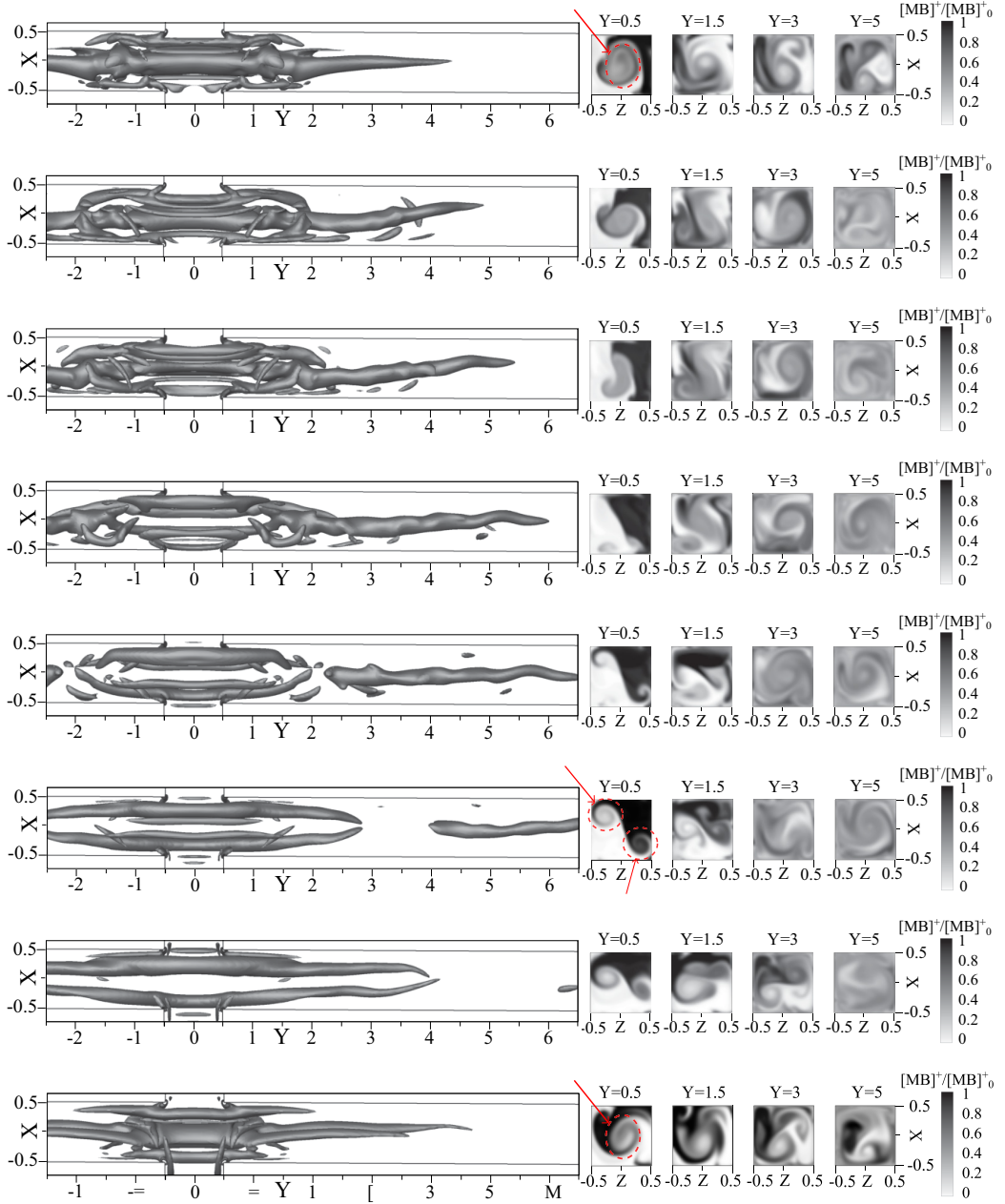
FIG. 2. Isosurfaces of the λ_2 vortex-indicator (left panel) and contours of the normalized methylene blue concentration in the outlet channel (right panel). Red dashed lines denote the vortex cores. Simulation at Re = 450 and [HCl] = 2.19 mol/l. Considered times: t/τ = 0, 0.125, 0.25, 0.375, 0.5, 0.625, 0.75, 0.875 (from top to bottom).

central vortex breaks in the confluence region and splits into two pairs of counterrotating vortices (clearly visible from the contours of MB$^+$ at $Y = 0.5$). At $t/\tau = 0.5$ only two of the four vortices survive in the confluence region. They are corotating and start to move towards each other between $t/\tau = 0.5$ and $t/\tau = 0.75$ (see again the contours of MB$^+$ at $Y = 0.5$). In the meanwhile, a blob
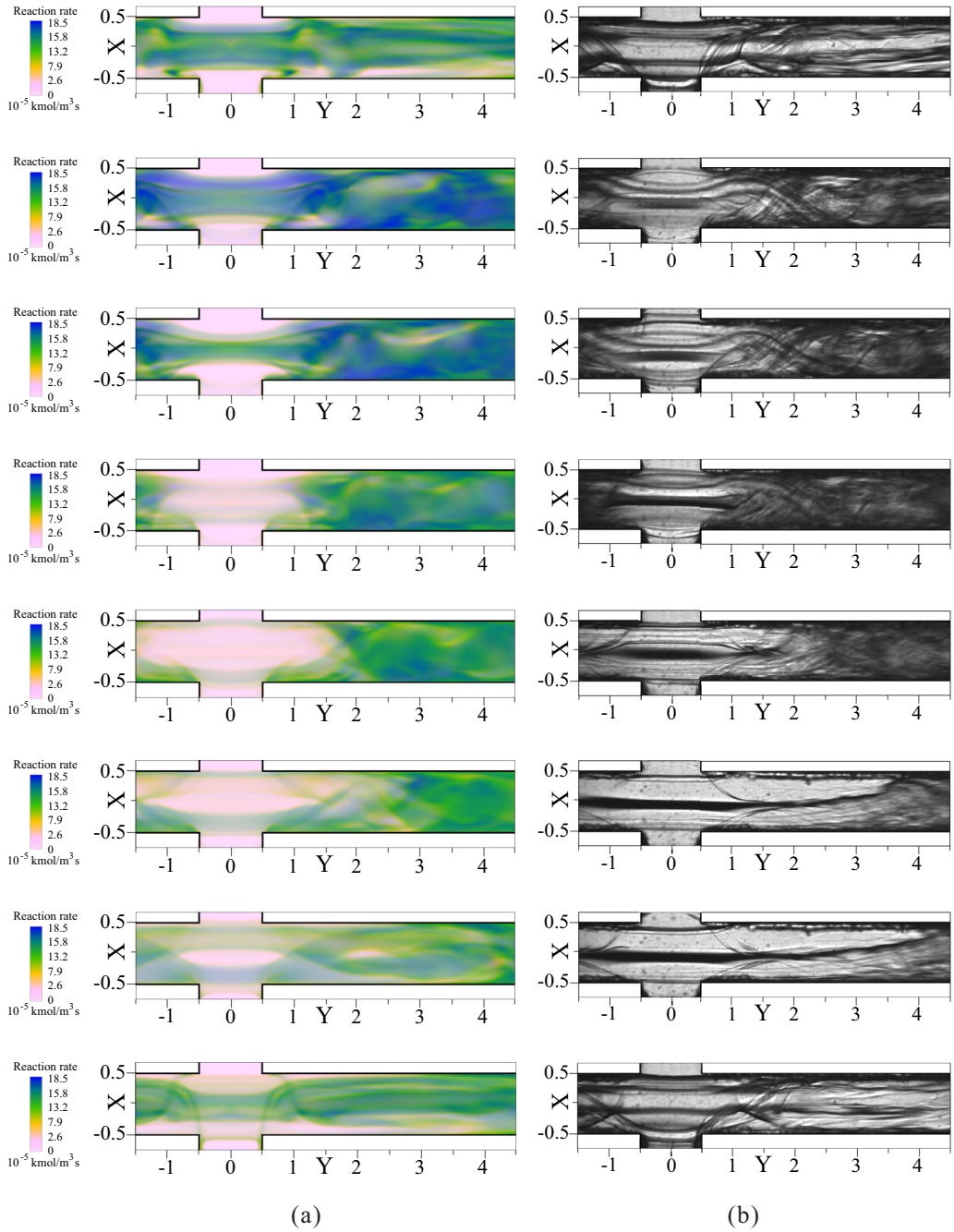
FIG. 3. Comparison between (a) numerical reaction-rate field and (b) experimental visualization of the contact area between AsA solution and water (b) at Re = 450 and [HCl] = 2.19 mol/l. Considered times: $t/\tau = 0, 0.125, 0.25, 0.375, 0.5, 0.625, 0.75, 0.875$ (from top to bottom). For the video of numerical reaction-rate field, see Supplemental Material [48]. For the video of experimental visualization of the contact area between AsA solution and water, see Supplemental Material [48].
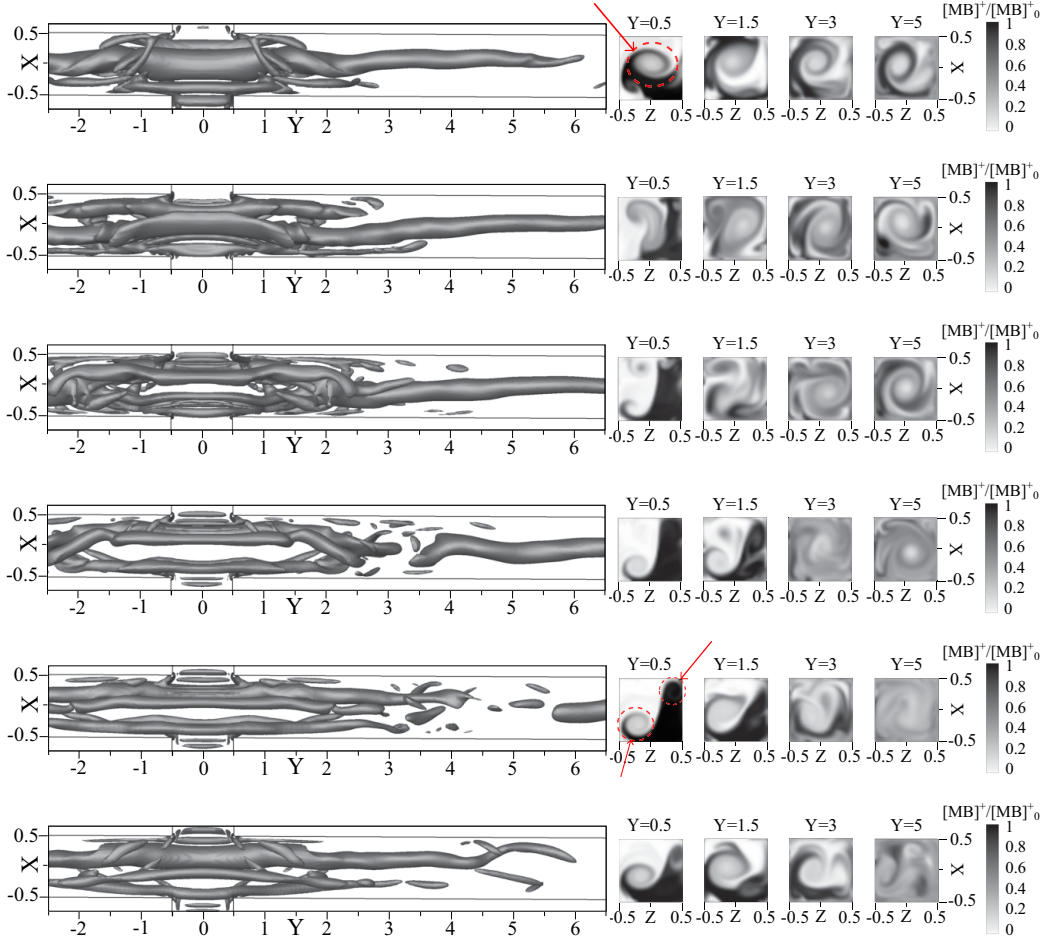
FIG. 4. Isosurfaces of the λ_2 vortex-indicator (left panel) and contours of the normalized methylene blue concentration in the outlet channel (right panel). Red dashed lines denote the vortex cores. Simulation at Re = 600 and [HCl] = 2.19 mol/l. Considered times: $t/\tau = 0$, 0.167, 0.333, 0.5, 0.667, 0.833 (from top to bottom).

of *y* vorticity, originating as previously described, is symmetrically convected along the two outlet channels. At $t/\tau = 0.875$ the two corotating lateral vortices approach each other and merge, forming again the central vortex.

Insights into the reaction features in the outlet channels can be obtained through the analysis of the numerical depth-averaged fields of reaction rate given in Fig. 3(a). The reaction rate corresponds to $\dot{\omega}_{MB^+}$, which is the rate of consumption of the methylene blue. Experimental flow visualizations are shown in Fig. 3(b) to give a qualitative glance of the contact fronts between the ascorbic acid and the methylene blue solutions. Indeed, the changes in the shade of grey are due to the different refractive indexes of the two reactive streams, highlighting thus the contact zones. As previously, for both numerical simulations and experiments, the results are reported at equally spaced times within the characteristic time cycle. Regarding the cycle duration, the corresponding Strouhal number in the experiments is equal to 0.057 at Re = 450, thus in excellent agreement with the numerical one. The comparison of the fields of reaction rate with the experimental visualizations confirms that the chemical reaction mainly takes place at the contact fronts between the two streams, which are in turn related to the three-dimensional vortical structure and their dynamics [see Fig. 2(a)], as already
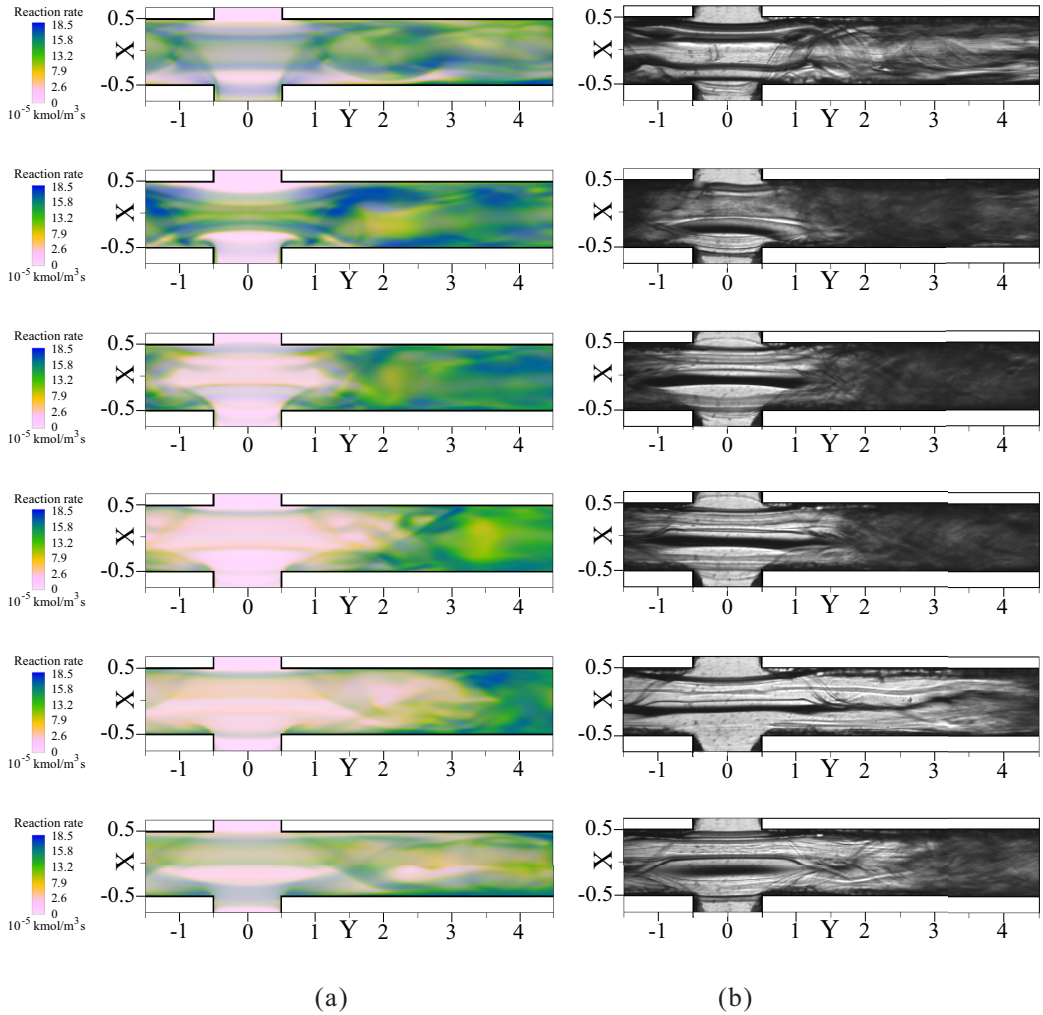
FIG. 5. Comparison between (a) numerical reaction-rate field and (b) experimental visualization of the contact area between AsA solution and water (right panel) at Re = 600 and [HCl] = 2.19 mol/l. Considered times: $t/\tau = 0, 0.167, 0.333, 0.5, 0.667, 0.833$ (from top to bottom).

found in the steady regimes in Ref. [41]. Indeed, during the cycle, the maximum reaction rate in the confluence region is obtained between $t/\tau = 0$ and $t/\tau = 0.125$, when the central vortex is present. At $t/\tau = 0.25$ the reaction rate in the confluence region starts to reduce, whereas it remains very high in the outlet channels thanks to the vorticity blob that is moving towards the outlet. This effect is even more evident at $t/\tau = 0.375$, with a sudden drop of reaction rate in the confluence due to the breakup of the central vortex but with a still high rate in the outlet channel. Between $t/\tau = 0.5$ and $t/\tau = 0.875$, the reaction rate in the confluence region is even lower because the two corotating vortices are less effective in mixing the reagents compared to the central vortex.

By further increasing Re, the previously described time-periodic regime is observed up to Re = 600 without significant changes in the flow pattern, as can be seen by comparing the results obtained at Re = 600 in Fig. 4 with the ones at Re = 450 in Fig. 2. The numerical depth-averaged fields of reaction rate and the corresponding experimental visualizations of the contact fronts between ascorbic acid solution and water are presented in Figs. 5(a) and 5(b). Six equally spaced instants in
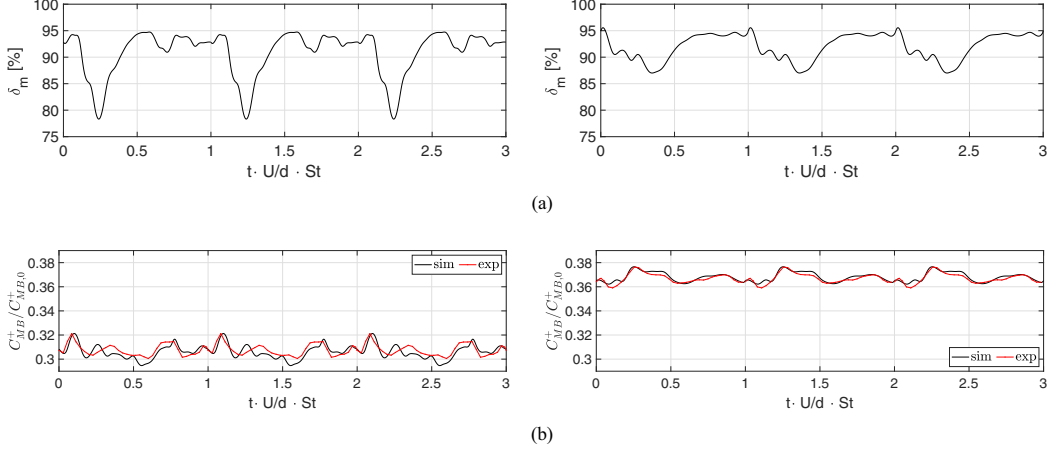
FIG. 6. (a) Numerical time behaviors of the degree of mixing and (b) comparison between experimental and numerical time behaviors of the normalized MB$^+$ concentrations, $C_{\text{MB}^+}/C_{\text{MB}^+,0}$. The results are evaluated at $Y = 25$ cross-section for Re = 450 (left panel) and Re = 600 (right panel).

the time period are reported in Figs. 4 and 5. For this Reynolds number, the time duration of the dynamic cycle is such that St = 0.07 in the simulations and St = 0.064 in the experiments, again in very good agreement. The vortical structures at Re = 600 are more elongated into the outlet channels than those at Re = 450 and, higher values of the reaction rate field occur when the central vortex is present in the confluence region because it leads to higher mixing between the two streams.

It is worth to remark that the described flow dynamics is significantly different from that found for T-mixers (see, e.g., Ref. [45]). In particular, T-mixers are characterized by two different unsteady regimes, the asymmetric and the symmetric one. In the symmetric regime, the flow recovers a dual mirror symmetry within the mixing channel, resulting in a significant reduction in mixing efficiency.

V. MIXING DEGREE AND REACTION YIELD

The degree of mixing δ_m is defined as in Refs. [22,40]:

$$\delta_m = 1 - \frac{\sigma_b}{\sigma_{\max}}, \tag{13}$$

where σ_b is the volumetric flow standard deviation on a cross-section S and $\sigma_{\max}$ is the maximum value of σ_b.

$$\sigma_b^2 = \frac{\int_S (\phi - \bar{\phi}_b)^2 \rho u_y dS}{\int_S \rho u_y dS}, \tag{14}$$

$$\sigma_{\max} = \sqrt{\bar{\phi}_b (1 - \bar{\phi}_b)}, \tag{15}$$

where u_y is the y component of the velocity, $\bar{\phi}_b$ is the bulk mass fraction. The degree of mixing varies between 0 (absence of mixing) and 1 (complete mixing).

The time behaviors of the degree of mixing and the normalized MB$^+$ concentrations are shown in Fig. 6 at $Y = 25$ cross-section for Re = 450 and Re = 600. The temporal signals of the δ_m is evaluated from numerical simulations [Fig. 6(a)], while Fig. 6(b) verifies the agreement between experiments and simulations in terms of the normalized MB$^+$ concentrations. Three cycles are presented, and the initial time is arbitrarily chosen as in Figs. 2 and 4. As previously said, the flow is well-mixed during the cycle, and the higher δ_m values are found when the single central vortex is present. On the contrary, its breakup leads to a sudden decrease in the mixing degree, as can be
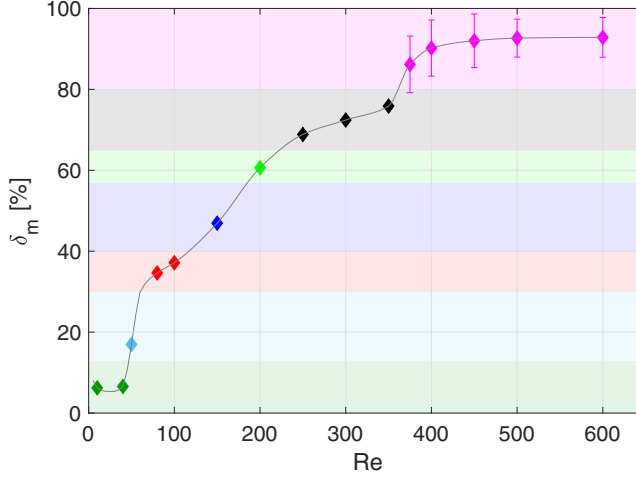
FIG. 7. Mixing degree numerically evaluated at $Y = 25$ as a function of the Reynolds number. The results are visually distinguished by color, considering those that fall within a mixing degree range of ± 4–7%.

seen, e.g., at $t/\tau = 0.25$ in the left panel of Fig. 6(a). By further increasing Reynolds, the two inlet streams are well-mixed along the outlet channel, as can be seen also at the $Y = 5$ cross-section in Fig. 4. This leads to a small variation of both δ_m and $C_{MB^+}/C_{MB^+,0}$ during the cycle time.

The mean value during the cycle and the standard deviation of δ_m computed numerically at $Y = 25$ are shown in Fig. 7 as a function of the Reynolds number. For the purpose of the analysis in Sec. VI, the results are subdivided by using different colors for the cases with similar values of δ_m, as can be seen from the different background colors of the Fig. 7. In particular, the data have been grouped, considering similar those within a mixing degree range of ± 4–7%. To better highlight this correspondence, Table II shows the different colors and their corresponding range of δ_m. As described in Ref. [41], the onset of the steady engulfment regime promotes the mixing of the streams, leading to a sudden increase in δ_m at Re $= 50$. The same behavior happens at the onset of the unsteady engulfment regime at Re $= 375$. The best performance in terms of mixing is achieved between Re $= 450$ and Re $= 600$, with $\delta_m \simeq 92\%$. Additionally, it is worth noting that the trend of mixing in the unsteady regimes differs from what observed for T-mixers, in which a sudden drop of δ_m with increasing Re occurs at the onset of the symmetric unsteady regime (see, e.g., Refs. [18,49]).

TABLE II. Correspondence between colors and values of the mixing degree.

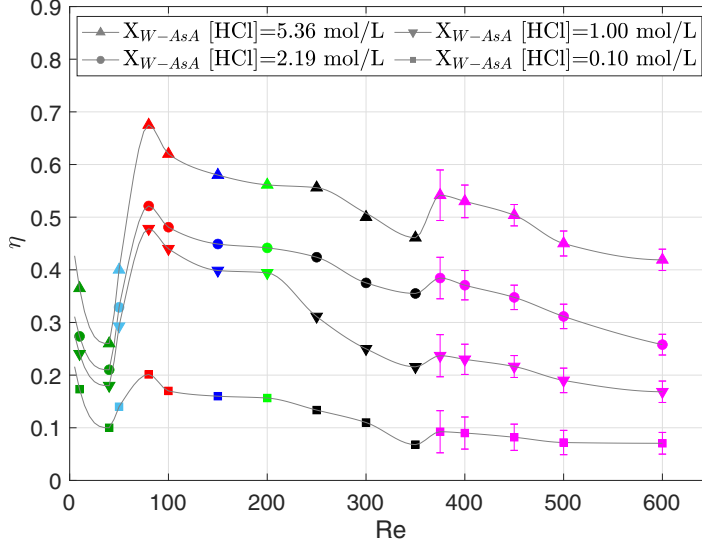| Colors	Range of δ_m [%]
I-dark green	<13
II-light blue	13–30
III-red	30–40
IV-blue	40–57
V-green	57–65
VI-black	65–80
VII-magenta	>80

FIG. 8. The reaction yield numerically evaluated at $Y = 25$, plotted as a function of Reynolds number. The computational results are color-coded based on the mixing degree levels defined in Fig. 7 and Table II.

At $\mathrm{Re} = 450$, the normalized concentration of MB^+ is always lower than at $\mathrm{Re} = 600$, thus the reaction efficiency is higher. To quantify this result, the reaction yield is evaluated as

$$\eta = 1 - 2\frac{C_{MB^+,Y}}{C_{MB^+,0}}, \qquad (16)$$

where $C_{MB^+,Y}$ is the methylene blue concentration averaged over Y and time. $C_{MB^+,0}$ is the averaged methylene blue concentration at the inlet.

Figure 8 shows the reaction yield as a function of the Reynolds number for four different HCl concentrations. As previously said, the flow features and the mixing degree are nearly independent of [HCl], which is a catalyst for the reaction and influences, thus, the product concentrations and the reaction yield. Despite the different concentrations of the catalyst lead to different quantitative values, the behavior of the reaction yield is the same for all the considered [HCl]. At low Reynolds numbers in the stratified regime, the reaction yield decreases as the Reynolds number increases. At the onset of the engulfment regime, the reaction yield suddenly increases, reaching its maximum at $\mathrm{Re} = 80$. Subsequently, the yield decreases with Re, although less steeply than in the stratified regime, because the increase of mixing with Re shown in Fig. 7 is not able to completely counterbalance the reduction of residence time due to the increased bulk velocity. The onset of the unsteady regime at $\mathrm{Re} = 375$ produces again an increase in yield due to the corresponding sudden increase in mixing degree. However, by further increasing Re within the unsteady regime, although the mixing between the streams remains high, the reduction of the residence time prevails, resulting in a decline in reaction yields.

VI. DEVELOPMENT OF AN ANALYTIC MODEL DESCRIBING THE X-MICROREACTOR PERFORMANCE

Figure 9 shows the reaction yield numerically evaluated at the cross-section at $Y = 25$ as a function of Damköhler number. The different panels refer to the four different catalyst concentrations, and, thus, to different chemical kinetic characteristic times. The symbols and colors are the same as in Fig. 8. The correlations proposed in Ref. [41] for the steady regimes are also reported. In particular, up to the onset of the engulfment regime it was found that $\eta \propto \mathrm{Da}^{0.3}$ for all the reaction
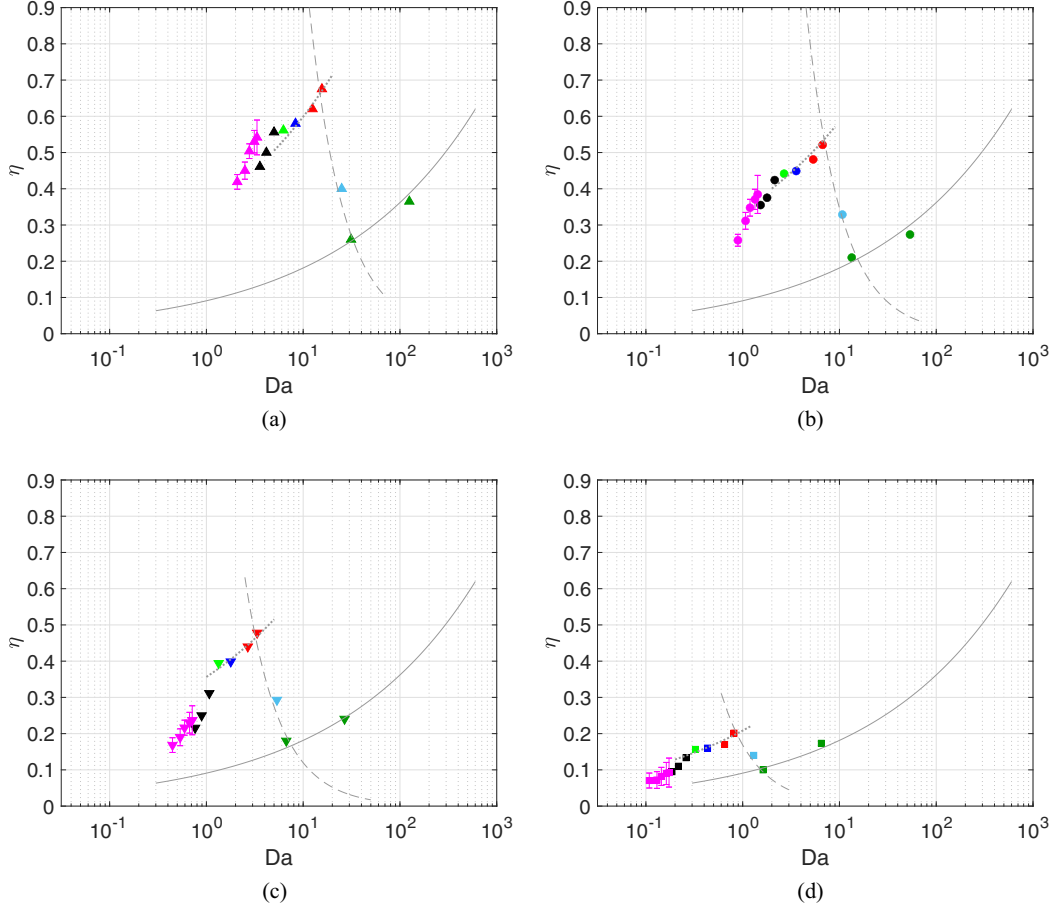
FIG. 9. Reaction yield numerically evaluated at $Y = 25$ cross-section as a function of Damköhler number. Considered cases: (a) [HCl] = 5.36 mol/l, (b) [HCl] = 2.19 mol/l, (c) [HCl] = 1.00 mol/l, and (d) [HCl] = 0.10 mol/l. Markers represent numerical results. The solid and dotted lines scale as $Da^{0.3}$, while the dashed one the scaling in Eq. (17).The results are colored according to the mixing degree levels defined in Fig. 7 and in Table II.

rates. The same holds also for T-reactors [40]. The solid lines represent indeed $Da^{0.3}$. It can be seen how the values of η obtained in the segregated regime (high values of the Damköhler and low values of mixing degree) closely follow the scaling. Conversely, in the engulfment regime Tomasi Masoni *et al.* [41] found that the reaction yield depends also on the reaction rate as follows:

$$\eta \propto \left(\frac{\tilde{k}_r^{0.1}}{Da^{0.4}} \right)^3, \tag{17}$$

where $\tilde{k}_r = k_r d^2 / \nu$ is a nondimensional kinetic constant. The dashed lines in Fig. 9 show the scaling of Eq. (17). It can be seen that this scaling holds only up to a value of Da, which corresponds to Re = 80 (see Fig. 9). After this Reynolds, for the rest of the steady engulfment regime, the data are fitted again by a curve proportional to $Da^{0.3}$, shifted compared with the one fitting the yields in the segregated regime. Finally, for all the reaction rates, the behavior in the unsteady regimes clearly deviate from both scalings [proportionality to $Da^{0.3}$ and Eq. (17)].
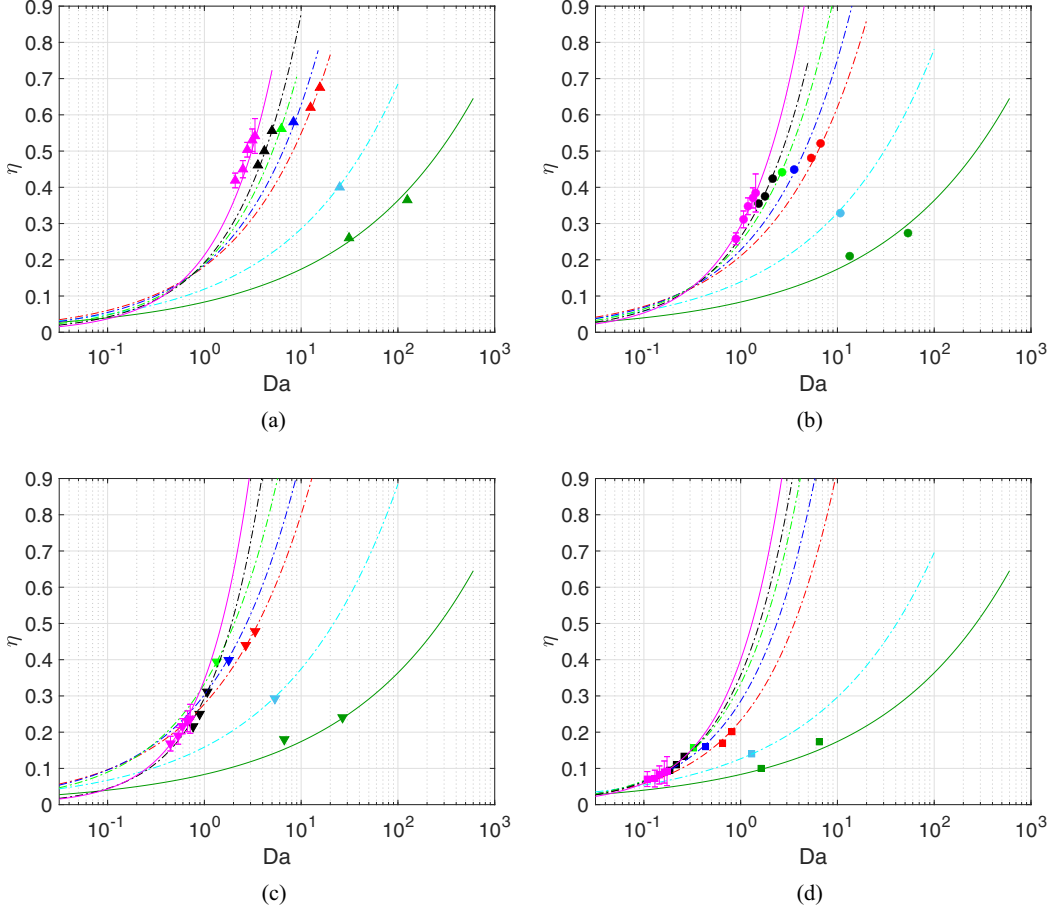
FIG. 10. Reaction yield numerically evaluated at $Y = 25$ cross-section as a function of Damköhler number. Considered cases: (a) [HCl] = 5.36 mol/l, (b) [HCl] = 2.19 mol/l, (c) [HCl] = 1.00 mol/l, and (d) [HCl] = 0.10 mol/l. Markers represent numerical results and lines represent Eq. (18). The results are colored according to the mixing degree levels defined in Fig. 7 and in Table II.

Instead of proposing a further interpolation of the data with $\tilde{k}_r$ and Da for the unsteady regimes, we try herein to find a new scaling of η based on Da and the degree of mixing. From a physical viewpoint, these parameter can be assumed as main factors affecting the reaction yield, as the first represents the ratio between the characteristic times of convection and chemistry and the second is directly linked with the extent of the contact surface between the two streams at which the reaction mainly occurs. To this aim, we analyze the data characterized by similar values of δ_m, which have the same color in Figs. 9. Figures 10(a)–10(d), reporting the same data as in Fig. 9, show that each group of yield values having similar δ_m (same color) is well interpolated by an exponential function of Damköhler. The exponent clearly varies for the different groups having similar δ_m. Therefore, we propose the following scaling for the reaction yield:

$$\eta \propto \mathrm{Da}^{\alpha+0.3}, \tag{18}$$

in which the exponent, α, varies with δ_m. Let us analyze first the dependence of α on δ_m for Da > 1, i.e., when the convection characteristic time is larger than the chemical one. All cases in Figs. 10(a) and 10(b) fall, e.g., in this category. For fixed δ_m (symbols of same color), by comparing the different
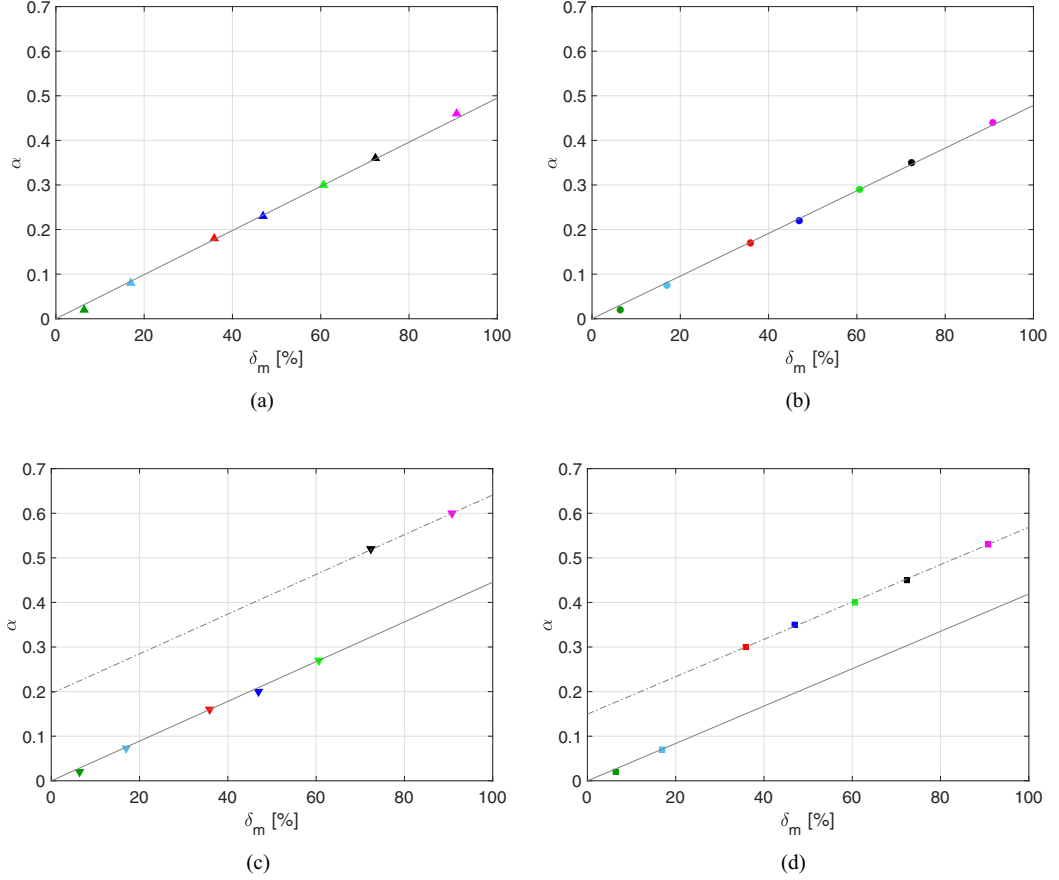
FIG. 11. (a) Parameter α as a function of the mixing degree. Considered cases: (a) [HCl] = 5.36 mol/l, (b) [HCl] = 2.19 mol/l, (c) [HCl] = 1.00 mol/l, and (d) [HCl] = 0.10 mol/l. The computational results are colored according to the mixing degree levels defined in Fig. 7 and in Table II.

panels of Fig. 10, relative to the different concentrations of HCl and, thus, to the different nominal chemical kinetic constants, it can be noticed that for the cases with Da > 1 the exponent remains roughly constant. Moreover, we expect α to increase with mixing, i.e., with δ_m, and when δ_m tends to zero (segregated regime), the scaling with $\text{Da}^{0.3}$ has to be recovered. Thus, we assume α to be proportional to δ_m. Figure 11 shows the behavior of α obtained by best-fitting the data in Fig. 10 as a function of δ_m. It is evident that, for cases having Da > 1, lying on solid straight lines, the dependence of α is linear with δ_m, i.e., $\alpha = m\delta_m$, with m roughly independent of the reaction rate. Conversely, when the nominal Damköhler becomes $\leqslant 1$, Figs. 11(c) and 11(d) show that α varies again linearly with δ_m, with the same slope as for Da > 1, but the straight line interpolating the data for Da < 1 is shifted towards higher values of α for a given δ_m. This change in the behavior is expected because when Da < 1, having a larger α leads to a reduced yield. This is physically sound because for Da < 1, i.e., when the fluid dynamic characteristic time becomes lower than the chemical one, the yield is expected to be lower than for Da > 1, independently of mixing. Based on these considerations, we propose the following expression for α:

$$\alpha = \begin{cases} m\delta_m & \text{if Da} > 1, \\ m\delta_m + q & \text{if Da} \leqslant 1. \end{cases} \quad (19)$$
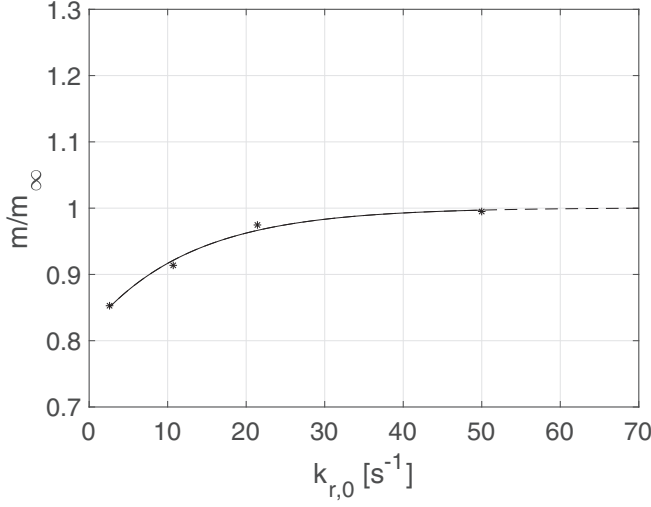
FIG. 12. Coefficient m/m_∞ as a function of the kinetic constant $k_{r,0}$.

As previously said, we expect m to be almost independent of $k_{r,0}$. To check this assumption, the coefficient m has been computed as a function of $k_{r,0}$ by best-fitting the data. The resulting expression is the following, which is also shown in Fig. 12:

$$m = m_\infty(1 - 0.1841e^{-0.0786\,k_{r,0}}), \tag{20}$$

with m_∞ being the slope of the curve $\alpha - \delta_m$ in the limit case $k_{r,0}$ tends to infinity, i.e., $m_\infty = 0.005$. Note that $m = m_\infty$ is an acceptable approximation except for the case of the slowest reaction, confirming, thus, our assumption. It should be also noted that q reduces by decreasing $k_{r,0}$ as expected for Da $\leqslant 1$ because the chemical reaction characteristic time is the dominating factor. In particular, we found $q = 0.2$ and $q = 0.145$ for $k_{r,0}$ equal to 10.71 s^{-1} and 2.60 s^{-1}, respectively. We are not proposing any analytic best-fitting since only two values of $q = q(k_{r,0})$ are available. We remark that cases for which Da < 1 are a priori less interesting because a low yield is expected, since the fluid dynamic residence time is lower compared to that of the reaction.

Finally, the lines reported in Fig. 10 are computed from Eqs. (18) and (19) for the different cases; the proportionality constant in Eq. (18) is adjusted to fit the data. It can be seen that the proposed scaling law is able to predict the yield in all the flow regimes (included the unsteady engulfment one) and for all the Damköhler numbers (chemistry slower and faster than flow convection), given the mixing degree and the nominal kinetic constant as input data.

VII. CONCLUSIONS

In the first part of the paper, the flow features of the periodic unsteady engulfment regime, occurring in the considered X-microreactor for Re $\geqslant 375$, have been described for the first time through joint experiments and numerical simulations. This regime is characterized by the presence of a central vortex (with two lateral corotating vortices), which periodically collapses leading to symmetric vorticity shedding in both outlet channels. In the meanwhile, two counterrotating vortices form in the confluence region, they come closer and merge forming again the central vortex. Compared with the steady engulfment regime previously described in Ref. [41], characterized by a single steady central vortex, the unsteady regime exhibits a higher mixing degree. However, the reaction yield remains comparable, because the increased mixing is counterbalanced by the reduction of the residence time because of the higher Reynolds numbers. This behavior is remarkably different from that of T-reactors, which are characterized by two distinct unsteady regimes, asymmetric and

symmetric. In the latter, occurring at larger Reynolds numbers than the asymmetric regime, the flow recovers a double mirror symmetry. Consequently, the mixing degree and the reaction yield show a remarkable drop at the onset of the symmetric regime. However, previous studies for T-mixers [18,42] showed that the aspect ratio of the channels may have a significant impact of the flow regimes and, hence, the mixing. Therefore, the impact of the shape of the channel cross-section for X-reactors is, in our opinion, worth investigating in the future. Conversely, we do not expect a major impact of different viscosity and density of the operating fluids in the unsteady regime. This is based on the findings in Ref. [20], for the same X-mixer geometry operated with water and ethanol in steady flow regimes, showing that the effects of different fluid density and viscosity are significant only at very low Reynolds numbers in the segregated regime.

Then, we observed that the scalings proposed in Ref. [41] for the reaction yield in the steady engulfment regime for the same X-mixer and the same reaction do not hold in the unsteady engulfment regime. Therefore, by analyzing the data obtained in the present study, a new scaling has been proposed with the aim of predicting the reaction yield for all the flow regimes. Compared with the model proposed in Ref. [41], which computes the reaction yield as a function of the Damköhler number and of the reaction kinetic constant, the proposed law explicitly takes into account the effect of the mixing degree, which we believe is the second key parameter influencing the reaction yield. Indeed, the mixing degree is directly linked with the extent of the contact surface between the flow streams at which the reaction mainly occurs, and, thus, it has a major impact on the reaction yield. The proposed model can satisfactorily predict the reaction yield in all the flow regimes (including the unsteady engulfment one) and for all the considered Damköhler numbers (i.e., $10^{-1} < Da < 10^3$), given the mixing degree and the nominal kinetic constant as input data. The proposed scalings might hold also for X-mixers having different shapes of the channel cross-section, since we may expect that the physical mechanisms linking the flow topology and dynamics, mixing, and reaction yield remain qualitatively similar. This will be, however, checked in future work.

---

[1] K. Elvira, X. C. I. Solvas, R. C. Wootton, and A. J. Demello, The past, present and potential for microfluidic reactor technology in chemical synthesis, Nat. Chem. **5**, 905 (2013).

[2] D. M. Roberge, L. Ducry, N. Bieler, P. Cretton, and B. Zimmermann, Microreactor technology: A revolution for the fine chemical and pharmaceutical industries? Chem. Eng. Technol. **28**, 318 (2005).

[3] H. Gemoets, Y. Su, M. Shang, V. Hessel, R. Luque, and T. Noel, Liquid phase oxidation chemistry in continuous-flow microreactors, Chem. Soc. Rev. **45**, 83 (2016).

[4] N. Kockmann, P. Thenée, C. Fleischer-Trebes, G. Laudadio, and T. Noël, Safety assessment in development and operation of modular continuous-flow processes, React. Chem. Eng. **2**, 258 (2017).

[5] C.-Y. Lee and L.-M. Fu, Recent advances and applications of micromixers, Sensors Actuators B: Chem. **259**, 677 (2018).

[6] N.-T. Nguyen and Z. Wu, Micromixers—A review, J. Micromech. Microeng. **15**, R1 (2005).

[7] F. Fanelli, G. Parisi, L. Degennaro, and R. Luisi, Contribution of microreactor technology and flow chemistry to the development of green and sustainable synthesis, Beilstein J. Org. Chem. **13**, 520 (2017).

[8] E. Sackmann, A. Fulton, and D. Beebe, The present and future role of microfluidics in biomedical research, Nature (London) **507**, 181 (2014).

[9] C. Liu, Y. Li, and B.-F. Liu, Micromixers and their applications in kinetic analysis of biochemical reactions, Talanta **205**, 120136 (2019).

[10] H. Shi, K. Nie, B. Dong, M. Long, H. Xu, and Z. Liu, Recent progress of microfluidic reactors for biomedical applications, Chem. Eng. J. **361**, 635 (2019).

[11] L. Capretto, D. Carugo, S. Mazzitelli, C. Nastruzzi, and X. Zhang, Microfluidic and lab-on-a-chip preparation routes for organic nanoparticles and vesicular systems for nanomedicine applications, Adv. Drug Deliv. Rev. **65**, 1496 (2013).

[12] N. Kimura, M. Maeki, Y. Sato, Y. Note, A. Ischida, H. Tani, H. Harashima, and M. Tokeshi, Development of the iLiNP device: Fine tuning the lipid nanoparticle size within 10 nm for drug delivery, ACS Omega **3**, 5044 (2018).

[13] Z. Liu, F. Fontana, A. Python, J. T. Hirvonen, and H. A. Santos, Microfluidics for production of particles: Mechanism, methodology, and applications, Small **16**, 1904673 (2020).

[14] I. Rossetti and M. Compagnoni, Chemical reaction engineering, process design and scale-up issues at the frontier of synthesis: Flow chemistry, Chem. Eng. J. **296**, 56 (2016).

[15] M. Jiang and R. D. Braatz, Designs of continuous-flow pharmaceutical crystallizers: Developments and practice, Cryst. Eng. Commun. **21**, 3534 (2019).

[16] N. Ait Mouheb, D. Malsch, A. Montillet, C. Solliec, and T. Henkel, Numerical and experimental investigations of mixing in T-shaped and cross-shaped micromixers, Chem. Eng. Sci. **68**, 278 (2012).

[17] N. Ait Mouheb, A. Montillet, C. Solliec, J. Havlica, P. Legentilhomme, J. Comiti, and J. Tihon, Flow characterization in T-shaped and cross-shaped micromixers, Microfluidics and Nanofluidics **10**, 1185 (2011).

[18] S. Camarri, A. Mariotti, C. Galletti, E. Brunazzi, R. Mauri, and M. V. Salvetti, An overview of flow features and mixing in micro T and arrow mixers, Ind. Eng. Chem. Res. **59**, 3669 (2020).

[19] A. Mariotti, C. Galletti, E. Brunazzi, and M. V. Salvetti, Unsteady flow regimes in arrow-shaped micro-mixers with different tilting angles, Phys. Fluids **33**, 012008 (2021).

[20] M. Antognoli, S. Tomasi Masoni, A. Mariotti, R. Mauri, E. Brunazzi, and C. Galletti, Investigation on steady regimes in a X-shaped micromixer fed with water and ethanol, Chem. Eng. Sci. **248**, 117254 (2022).

[21] M. S. C. A. Brito, I. S. O. Barbosa, C. P. Fonte, M. M. Dias, J. C. B. Lopes, and R. J. Santos, Effective mixing of dissimilar fluids in asymmetric confined impinging jets mixers, Chem. Eng. Sci. **258**, 117756 (2022).

[22] C. Galletti, A. Mariotti, L. Siconolfi, R. Mauri, and E. Brunazzi, Numerical investigation of flow regimes in T-shaped micromixers: Benchmark between finite volume and spectral element methods, Can. J. Chem. Eng. **97**, 528 (2019).

[23] A. S. Lobasov and A. V. Minakov, Analyzing mixing quality in a T-shaped micromixer for different fluids properties through numerical simulation, Chem. Eng. Process. Process Intens. **124**, 11 (2018).

[24] A. Mariotti, M. Lanzetta, G. Dini, A. Rossi, E. Brunazzi, R. Mauri, and C. Galletti, Influence of cross-sectional geometry on mixing in a T-shaped micro-junction, Chem. Eng. Trans. **74**, 955 (2019).

[25] R. J. Poole, M. Alfateh, and A. P. Gauntlett, Bifurcation in a T-channel junction: Effects of aspect ratio and shear-thinning, Chem. Eng. Sci. **104**, 839 (2013).

[26] K. Krupa, M. A. Sultan, C. P. Fonte, M. I. Nunes, M. M. Dias, J. C. B. Lopes, and R. J. Santos, Characterization of mixing in t-jets mixers, Chem. Eng. J. **207-208**, 931 (2012).

[27] M. Sultan, K. Krupa, C. Fonte, M. Nunes, M. Dias, J. C. Lopes, and R. Santos, High-throughput T-jets mixers: An innovative scale-up concept, Chem. Eng. and Technol. **36**, 323 (2013).

[28] R. H. Liu, M. A. Stremler, K. V. Sharp, M. G. Olsen, J. G. Santiago, R. J. Adrian, H. Aref, and D. J. Beebe, Passive mixing in a three-dimensional serpentine microchannel, J. Microelectromech. Syst. **9**, 190 (2000).

[29] S. Hardt, H. Pennemann, and F. Schönfeld, Theoretical and experimental characterization of a low-Reynolds number split-and-recombine mixer, Microfluid. Nanofluid. **2**, 237 (2006).

[30] M. Antognoli, L. Donato, C. Galletti, D. Stoecklein, D. Di Carlo, and E. Brunazzi, Pre-arranged sequences of micropillars for passive mixing control of water and ethanol, Chem. Eng. J. **461**, 141851 (2023).

[31] M. Antognoli, S. Tomasi Masoni, A. Mariotti, R. Mauri, M. V. Salvetti, E. Brunazzi, and C. Galletti, Mixing improvement in a T-shaped micro-junction through small rectangular cavities, Micromachines **13**, 159 (2022).

[32] H. S. Santana, J. L. S. Júnior, and O. P. Taranto, Numerical simulations of biodiesel synthesis in microchannels with circular obstructions, Chem. Eng. Process.: Process Intens. **98**, 137 (2015).

[33] H. Wang, P. Iovenitti, E. Harvey, and S. Masood, Optimizing layout of obstacles for enhanced mixing in microchannels, Smart Mater. Struct. **11**, 662 (2002).

[34] P. G. Correa, J. R. Mac Intyre, J. M. Gomba, M. A. Cachile, J. P. Hulin, and H. Auradou, Three-dimensional flow structures in X-shaped junctions: Effect of the Reynolds number and crossing angle, Phys. Fluids **31**, 043606 (2019).

[35] S. J. Haward, R. J. Poole, M. A. Alves, P. J. Oliveira, N. Goldenfeld, and A. Q. Shen, Tricritical spiral vortex instability in cross-slot flow, Phys. Rev. E **93**, 031101 (2016).

[36] J.-W. Zhang, W.-F. Li, X.-L. Xu, H.-F. Liu, and F.-C. Wang, Experimental investigation of three-dimensional flow regimes in a cross-shaped reactor, Phys. Fluids **31**, 034105 (2019).

[37] J.-W. Zhang, T.-L. Yao, W.-F. Li, M. El Hassan, X.-L. Xu, H.-F. Liu, and F.-C. Wang, Trapping region of impinging jets in a cross-shaped channel, AIChE J. **66**, e16822 (2020).

[38] N. Burshtein, A. Q. Shen, and S. J. Haward, Controlled symmetry breaking and vortex dynamics in intersecting flows, Phys. Fluids **31**, 034104 (2019).

[39] A. Mariotti, M. Antognoli, C. Galletti, R. Mauri, M. V. Salvetti, and E. Brunazzi, Effects of flow unsteadiness and chemical kinetics on the reaction yield in a T-microreactor, Chem. Eng. Res. Design **179**, 1 (2022).

[40] A. Mariotti, M. Antognoli, C. Galletti, R. Mauri, M. V. Salvetti, and E. Brunazzi, The role of flow features and chemical kinetics on the reaction yield in a T-shaped micro-reactor, Chem. Eng. J. **396**, 125223 (2020).

[41] S. Tomasi Masoni, M. Antognoli, A. Mariotti, R. Mauri, M. V. Salvetti, C. Galletti, and E. Brunazzi, Flow regimes, mixing and reaction yield of a mixture in an X-microreactor, Chem. Eng. J. **437**, 135113 (2022).

[42] T. Andreussi, C. Galletti, R. Mauri, S. Camarri, and M. V. Salvetti, Flow regimes in T-shaped micro-mixers, Comput. Chem. Eng. **76**, 150 (2015).

[43] S. Mowry and P. Ogren, Kinetics of methylene blue reduction by ascorbic acid, J. Chem. Edu. **76**, 970 (1999).

[44] A. Mariotti, C. Galletti, R. Mauri, M. V. Salvetti, and E. Brunazzi, Effect of stratification on the mixing and reaction yield in a T-shaped micro-mixer, Phys. Rev. Fluids **6**, 024202 (2021).

[45] A. Mariotti, C. Galletti, R. Mauri, M. V. Salvetti, and E. Brunazzi, Steady and unsteady regimes in a T-shaped micro-mixer: Synergic experimental and numerical investigation, Chem. Eng. J. **341**, 414 (2018).

[46] M. Shamim and S. Khoo, Some physical properties of aqueous L-ascorbic acid solutions, Aust. J. Chem. **32**, 2293 (1979).

[47] J. Jeong and F. Hussain, On the identification of a vortex, J. Fluid Mech. **285**, 69 (1995).

[48] See Supplemental Material at http://link.aps.org/supplemental/10.1103/PhysRevFluids.9.024202 for (a) the video of experimental (b) visualization of the contact area between AsA solution and water at Re = 450 and [HCl] = 2.19 mol/l and the video of numerical reaction-rate field at Re = 450 and [HCl] = 2.19 mol/l.

[49] A. Mariotti, C. Galletti, M. V. Salvetti, and E. Brunazzi, Unsteady flow regimes in a T-shaped micromixer: Mixing and characteristic frequencies, Ind. Eng. Chem. Res. **58**, 13340 (2019).